Generating Far-Field Orbital Angular Momenta from Near-Field Optical Chirality

Yuri Gorodetski,[1] Aurélien Drezet,[2] Cyriaque Genet,[1,*] and Thomas W. Ebbesen[1]

[1]*ISIS, Université de Strasbourg, and CNRS (UMR 7006), 8 Allée Gaspard Monge, 67000 Strasbourg, France*
[2]*Institut Néel, CNRS, and Université Joseph Fourier (UPR 2940), 25 Rue des Martyrs, 38000 Grenoble, France*

(Received 5 December 2012; published 16 May 2013)

We demonstrate orbital angular momentum (OAM) transfer by chiral plasmonic nanostructures designed on both sides of a thin suspended metallic membrane. We show how far-field vortex beams with tunable OAM indices can be tailored through nanostructure designs. We reveal the crucial role played by the central aperture that connects the two sides of the membrane from which OAM selection rules are derived in perfect agreement with experimental data.

DOI: 10.1103/PhysRevLett.110.203906 PACS numbers: 42.79.Ag, 42.25.Ja, 42.50.Tx, 73.20.Mf

Structured light beams with phase or polarization singularities have revealed unique optical properties with applications ranging from super-resolution imaging to quantum optics [1–4]. Currently, chiral nanostructures draw promising routes for enhancing singular optical signatures with new functionalities in metamaterial science [5–7]. Interestingly, while the connection between optics and chirality is well established for three-dimensional (3D) chiral structures, the interaction of chiral light with 2D chiral objects is a topic of ongoing debate [8–10], with strong potential in physical chemistry for chirality enhancement in the near field [11–13].

Recently, singular optical effects have been discussed in the near field, in particular in relation to chiral surface plasmon (SP) modes which have been shown to carry orbital angular momentum (OAM) [14–17]. But until now, singular SP modes and associated spin-orbit coupling have only been probed in the near field [18–20]. Studies on plasmonic beaming with OAM have been scarce [21–23] and the relation between near-field chirality and OAM in the far field was never addressed.

In this Letter, we demonstrate that nanostructures carefully designed on both sides of a thin suspended membrane lead to tailoring optical OAM in the far field. Single and double-sided plasmonic structures consisting of concentric grooves periodically spaced from a central aperture—so-called plasmonic bull's eye (BE)—have shown extraordinary optical transmission and beaming effects [24,25]. Yet, the OAM behavior of these structures was not discussed. This Letter analyzes the OAM transfer during plasmonic incoupling and outcoupling by chiral nanostructures at each side of a membrane, stressing the role of a back-side structure in generating vortex beams as $e^{i\ell\varphi}$ with tunable OAM indices ℓ. We generate beams of light carrying OAM up to $|\ell| = 8$ and reveal the fundamental role of the central aperture through specific OAM selection rules.

Our device consists of a suspended thin ($h \sim 300$ nm) metallic membrane, fabricated by evaporating a metal film over a poly(vinyl formal) resin supported by a transmission electron microscopy copper grid. After evaporation, the resin is removed using a focused ion beam, leaving a gold membrane freely suspended in air. Shallow plasmonic structures are milled, in either concentric (BE) or spiral geometry on both sides of the membrane around a unique central cylindrical aperture acting as the sole transmissive element of the whole device—Fig. 1. The general groove radial path is given in the polar $(\hat{\boldsymbol{\rho}}, \hat{\boldsymbol{\varphi}})$ basis as $\boldsymbol{\rho}_n = (n\lambda_{\mathrm{SP}} + m\varphi\lambda_{\mathrm{SP}}/2\pi)\hat{\boldsymbol{\rho}}$, with n an integer, $0 \le \varphi \le 2\pi$, λ_{SP} the SP wavelength, and m a pitch number. A series of such grooves with consecutive index n defines a spiraling shallow grating on the metal surface with a radial periodicity of λ_{SP}—see Fig. 1(b). The definition of the radial path and handedness is fixed throughout this Letter with respect to the propagation direction of the incident light, meaning that the sign of the pitch m does not depend on the choice of the membrane side. With our conventions, a right-handed spiral R_m corresponds to $m > 0$ and a left-handed spiral L_m to $m < 0$.

The simple situation of a plasmonic BE structure ($m_{\mathrm{in}} = 0$) milled on the front side of a gold membrane and a spiral with a pitch of $m_{\mathrm{out}} = \pm 1$ on the back side is shown in Fig. 1. The membrane is illuminated by a single mode fiber pigtailed laser diode at $\lambda_0 = 785$ nm. The depth of the grooves (30 nm) is smaller than the skin depth ($\sim$70 nm at λ_0) so that no light can leak through the membrane—light can only be transmitted through the central hole perforating the membrane. The periodicity λ_{SP} of the spiraling groove is chosen with respect to λ_0 so that SP modes on the front side of the membrane are only excited efficiently by the plane wave component of the illumination beam normal to the membrane. The SP field propagates toward, and is transmitted through, the central hole. It is then decoupled to the far field by the periodic groove at the back side of the membrane, as a quasi-plane-wave. We start with an aperture of subwavelength diameter 400 nm that still provides sufficient signal-to-noise ratio when imaging the transmitted beam. We take a paraxial incoming beam $\mathbf{E}_{\pm}^{\mathrm{in}}(\boldsymbol{\rho}, z)e^{-i\omega t} = \hat{\boldsymbol{\sigma}}_{\pm}\mathcal{E}(\boldsymbol{\rho})e^{ik_z z}e^{-i\omega t}$ with an incident wave vector $k_z = 2\pi/\lambda_0$, in either the right ($\hat{\boldsymbol{\sigma}}_+$) or left ($\hat{\boldsymbol{\sigma}}_-$) circular

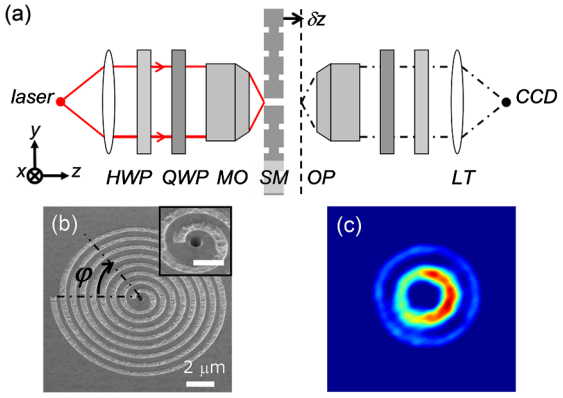

FIG. 1 (color online). (a) Experimental setup: the expanded incoming laser beam is circularly polarized using half- (HWP) and quarter-wave (QWP) plates. It is weakly focused on the nanostructured suspended membrane (SM) by a microscope objective (MO, 4×, NA = 0.13). The transmitted light is collected by a second objective (40×, NA = 0.60). A lens tube (LT, $f = 200$ mm) images the collection objective object plane (OP, dashed line) on a CCD camera, after additional HWPs and QWPs have analyzed the transmitted light in the circular polarization basis. (b) Scanning electron microscope image of a R_1 spiral milled on the Au membrane, with $m = 1$ and for $\lambda_{SP} = 768$ nm. Inset shows the central hole (scale bar is 1 μm). (c) Intensity distribution imaged through a BE-R_1 structure illuminated with a right circular polarization and analyzed with a left circular polarization. To image the interferograms (see main text), the OP is $\delta z = 20$ μm behind the membrane [28].

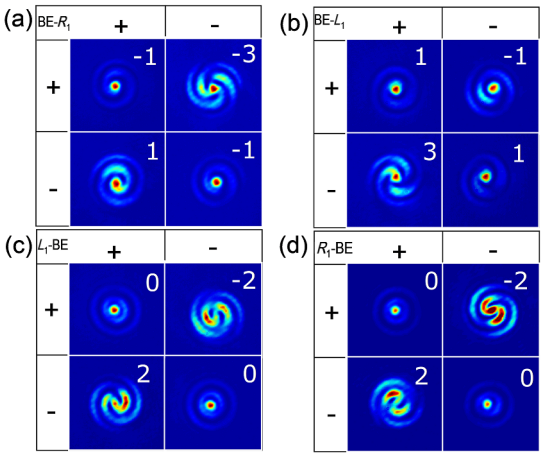

FIG. 2 (color online). Intensity distributions of the beam emerging from (a) BE-L_1, (b) BE-R_1, (c) R_1-BE, and (d) L_1-BE structures, respectively. The hole diameter used in all the structures is 400 nm. Labels ($\pm$, $\pm$) correspond to the combination of circular polarization preparation and analysis. The numbers give the corresponding OAM indices.

polarization state. The transmitted beam is analyzed in the same circular basis and images $\mathcal{M}_{ij}$ are recorded, with the four $(i, j) = (\pm, \pm)$ combinations of preparation j and analysis i.

Figure 2 displays such transmission images for membranes comprising a BE in the front side and alternatively L_1 and R_1 spirals on the back side. The spiraling structure of the images can be understood as a Fano-type interference between the spherical wave front of the light directly diffracted through the hole and the quasiplanar wave front of the vortex beam decoupled from the plasmonic nanostructure on the back side of the membrane [26,27]. Our system has, therefore, a built-in reference wave that generates interferograms imaged with the setup described in Fig. 1 [28]. The number of arms and handedness of the interferograms directly give the OAM index and sign $\pm\ell$ of the vortex beam [29,30]. OAM values of $\ell_{++} = \ell_{--} = -1$ and $\ell_{-+} = 1$ and $\ell_{+-} = -3$ are measured for the crossed terms shown in Fig. 2 for the BE-R_1 configuration, with signs merely reversed when a L_1 spiral is milled on the back side—Fig. 2(b).

Near-field generation of the OAM at the front side ($z = 0^+$) of the structured membrane can be modeled by considering that each point $\boldsymbol{\rho}_n$ of the groove illuminated by the incoming field is a SP point source, launching a SP wave perpendicularly to the groove. With groove widths much smaller than the illumination wavelength, the in-plane component of the generated SP field in the vicinity of the center of the structure is $\mathbf{E}^{SP}(\boldsymbol{\rho}_0, z = 0^+) \propto \mathsf{G} \cdot [\mathbf{E}^{in}(\boldsymbol{\rho}_n, z = 0^+) \cdot \hat{\mathbf{n}}_n]\hat{\mathbf{n}}_n$, where $\mathsf{G} = e^{ik_{SP}|\boldsymbol{\rho}_0 - \boldsymbol{\rho}_n|}/(|\boldsymbol{\rho}_0 - \boldsymbol{\rho}_n|)^{1/2}$ is the Huygens-Fresnel plasmonic propagator [31,32] and $\hat{\mathbf{n}}_n = \kappa^{-1}(d^2\boldsymbol{\rho}_n/ds^2)$ the local unit normal vector determined from the curvature κ and the arc length s of the groove.

The resultant SP field is the integral of elementary point sources over the whole groove structure. As indicated by a full evaluation, we can conveniently limit the integration to radial regions $\rho_n \gg \rho_0$, where the grooves become almost annular (see the Supplemental Material [33]). This leads to $\hat{\mathbf{n}}_n \sim -\hat{\boldsymbol{\rho}}$ and therefore to a simple expression of the integrated SP field $\mathbf{E}^{SP} \propto \sum_n \sqrt{n\lambda_{SP}} \int_0^{2\pi} d\varphi e^{im\varphi} \times e^{-ik_{SP}\rho_0 \cos(\varphi - \varphi_0)}[\mathbf{E}^{in}_{\pm} \cdot \hat{\boldsymbol{\rho}}]\hat{\boldsymbol{\rho}}$. By rewriting the polarization coupling term $[\mathbf{E}^{in}_{\pm} \cdot \hat{\boldsymbol{\rho}}]\hat{\boldsymbol{\rho}} = [\hat{\boldsymbol{\rho}} \otimes \hat{\boldsymbol{\rho}}] \cdot \mathbf{E}^{in}_{\pm}$, the $\otimes$ symbol denoting a dyadic product [34], the in-plane radially polarized SP near field is connected to the incoming field as $\mathbf{E}^{SP} = \mathsf{C}_{in} \cdot \mathbf{E}^{in}$ by an incoupling matrix

$$\mathsf{C}_{in}(m) \propto e^{im\varphi_0} \int_0^{2\pi} d\varphi e^{im\varphi} e^{-ik_{SP}\rho_0 \cos\varphi} \hat{\boldsymbol{\rho}} \otimes \hat{\boldsymbol{\rho}}. \quad (1)$$

The φ dependency of the circularly polarized illumination $\hat{\boldsymbol{\sigma}}_{\pm} = (\hat{\boldsymbol{\rho}} \pm i\hat{\boldsymbol{\varphi}})e^{\pm i\varphi}/\sqrt{2}$ that makes the integration (1) spin dependent is crucial. The excited SP field hence corresponds to a plasmonic vortex carrying OAM of $\ell_{SP} = m \pm 1$, depending on the incident $\hat{\boldsymbol{\varphi}}_{\pm}$ polarization, revealing spin-orbit coupling due to a radial plasmonic structure.

In contrast with recent studies confined to the near field [18–21], a new possibility is given here to decouple the singular near field into the far field with an additional structure on the back side of the suspended membrane

connected to the front side by the central hole. By symmetry (assuming loss-free unitarity) the outcoupling matrix is simply given as the Hermitian conjugate of the incoupling matrix, i.e., $\mathsf{C}_{\text{out}} = \mathsf{C}_{\text{in}}^{\dagger}$, corresponding to a surface field that propagates away from the central hole on the back side.

The incoupling-outcoupling sequence corresponds to the product $\mathsf{T} = \mathsf{C}^{\dagger}(m_{\text{out}}) \cdot \mathsf{C}(m_{\text{in}})$ which, in the circular polarization basis, writes explicitly as

$$\mathsf{T} \propto e^{i(m_{\text{in}} - m_{\text{out}})\varphi} \begin{bmatrix} \mathsf{t}_{++} & \mathsf{t}_{+-} e^{-2i\varphi} \\ \mathsf{t}_{-+} e^{2i\varphi} & \mathsf{t}_{--} \end{bmatrix}, \tag{2}$$

with t_{ij} radial functions (see the Supplemental Material [33]). This expression reveals two contributions: a polarization dependent geometric phase, within the matrix, that stems from the spin-orbit coupling at the annular groove, and a factorized dynamic phase that arises due to the spiral twist of the structure [20]. Note, that for $m_{\text{out}} = m_{\text{in}} = 0$, T describes a pure spin-orbit angular momentum transfer, conserving the total angular momentum [20,34–36]. We can cast in Table I these results as OAM summation rules. Remarkably, the measurements presented in Fig. 2 are in agreement with this table, demonstrating experimentally OAM transfer to the far field from the excitation of a chiral plasmonic near field at the back side of the membrane.

This analysis, however, does not exhaust the OAM generation process as it can be plainly seen when flipping the membrane. The OAM measurements obtained with a BE-$(L, R)_1$ structures and the (flipped) $(R, L)_1$-BE ones do not coincide, in contradiction with reciprocity operating on T. The OAM data obtained, e.g., for the L_1-BE configuration are shown in Fig. 2(d) and turn out inconsistent with the expectation values of Table I. Surprisingly since L_1 means $m_{\text{in}} = -1$, the agreement is reached only when fitting $m_{\text{in}} \equiv 0$ in the table. This discrepancy points to the pivotal role of the aperture in the process of OAM conservation.

As it is well known, a waveguide mode inside a hole of radius ρ_h and symmetry axis along the z direction is one term $J_\ell(k_{\ell n}\rho_h)e^{\pm i\ell\varphi}e^{\pm i\kappa_{\ell n}z}$ of a multipolar expansion, where J_ℓ is the ℓ-order Bessel function of the first kind and $\kappa_{\ell n}$ is the waveguide propagation wave vector [37]. This expansion shows that each ℓn waveguide mode carries an angular momentum $\pm\ell$. Boundary conditions, for transverse electric (TE) and transverse magnetic (TM) polarizations, fix cutoff hole diameters $d^c_{\ell n}$ at which the field propagates through the hole with a $\pm\ell$ OAM (see the Supplemental Material [33]). This aspect, so seldomly discussed in relation with the far-field transmission properties of cylindrical apertures [38], becomes central in our experiments.

TABLE I. Far-field summation rules for OAM generated through the membrane.

	+	−
+	$m_{\text{in}} - m_{\text{out}}$	$m_{\text{in}} - m_{\text{out}} - 2$
−	$m_{\text{in}} - m_{\text{out}} + 2$	$m_{\text{in}} - m_{\text{out}}$

Such OAM cutoff conditions mean that the hole only sustains waveguide modes excited by an incoming field carrying an angular momentum ℓ' that falls within the allowed OAM values ℓ determined by $d^c_{\ell n}$. The excitation field can either be $\mathbf{E}^{\text{in}}_{\pm}$ or the SP field launched by the grooves with $\mathbf{E}^{\text{SP}} = \mathsf{C}_{\text{in}}(m) \cdot \mathbf{E}^{\text{in}}_{\pm}$. With $E^{\text{in}}_z = 0$, $\mathbf{E}^{\text{in}}_{\pm}$ only excites a TE_{11} mode (higher modes can be excited under normal incidence only radial or azimuthal polarizations) [39,40]. In contrast, the launched SP field, scattered on the hole edges, can excite both TE and TM waveguide modes.

The angular momentum ℓ' carried by $\mathbf{E}^{\text{in}}_{\pm}$ is determined from the spin of light $\ell'_\sigma = \pm 1$. The SP field $\mathbf{E}^{\text{SP}}$ carries $\ell'_{\text{SP}} = m \pm 1$ from the near-field spin-orbit coupling described in Eq. (1). Accordingly, an OAM selection rule can be derived from an overlap integral between the excitation and the waveguide fields as

$$\mathcal{O}_{n\ell\ell'} = \alpha_\ell(k_{\ell n})\delta_{\ell,\ell'}, \tag{3}$$

where $\alpha_\ell(k_{\ell n})$ equals the radially integrated value (see the Supplemental Material [33]).

The discussion leads to the definition of an effective matrix $\mathsf{H}_{\ell n}$ for the hole that connects the front side ($z = 0^+$) and the back side ($z = h$) of the membrane while simultaneously accounting for OAM transfer from one side to the other (see the Supplemental Material [33]). Because the hole is the only optical element in the system that connects both the far and near fields from both sides of the membrane, the whole OAM generation in the far-field transmission process is described through a product matrix $\mathsf{T} = [\mathsf{C}(m_{\text{out}}) + \mathsf{I}_{\text{out}}]^{\dagger} \cdot \mathsf{H}_{\ell n} \cdot [\mathsf{I}_{\text{in}} + \mathsf{C}(m_{\text{in}})]$. With I proportional to the identity matrix, the $\mathsf{I}_{\text{out}} \cdot \mathsf{H}_{\ell n} \cdot \mathsf{I}_{\text{in}}$ channel corresponds to the direct path yielding the Fano-type far-field interferograms. As usual, we will assume that when they can be excited, the channels that involve C operators are resonantly enhanced over the direct illumination I_{in} or direct diffraction I_{out} ones.

Let us analyze precisely the OAM cutoff conditions corresponding to our experimental conditions. The fundamental waveguide mode in the central aperture is the TE_{11} mode at which the hole sustains an OAM index $|\ell| = 1$. At λ_0, we evaluate the cutoff diameter for the TM_{01} as $d^c_{01} = 580$ nm. For a diameter $d_h \geq d^c_{01}$, the hole can thus sustain, in addition to $|\ell| = 1$, another OAM index of 0. An OAM index of ± 2 will be allowed above the TE_{21} cutoff diameter found at $d^c_{21} = 740$ nm. A full agreement between Table I and the experimental results is reached when combining this dimension analysis with the selection rules derived above.

This is seen in the data gathered in Fig. 3 for the L_1-BE structure. The (i, j) interferograms monitor the evolution of the OAM generation as a function of cutoff conditions.

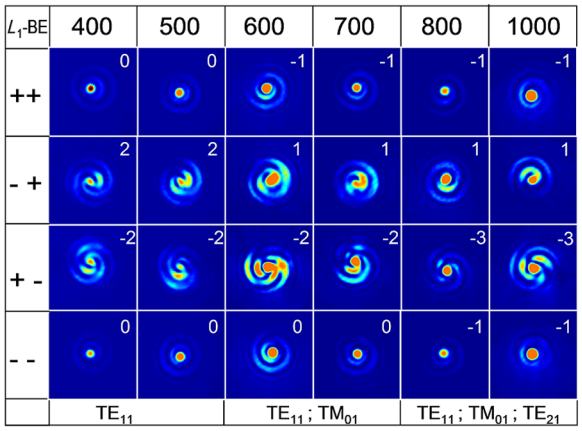

FIG. 3 (color online). Intensity (normalized) distributions measured through an L_1-BE structure as a function of hole diameters (first line, d_h in nm) and associated allowed waveguide modes (bottom line). Same notations as in Fig. 2.

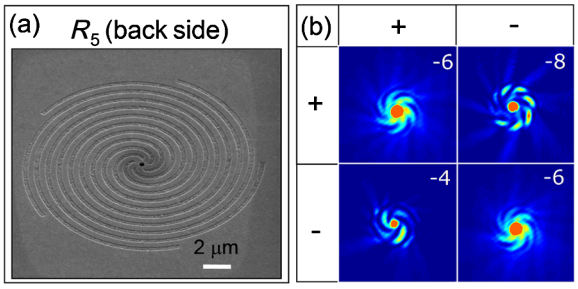

FIG. 4 (color online). (a) Scanning electron microscope image of an R_5 spiral milled on the back side of a membrane. (b) Intensity (normalized) distributions measured through an L_1-R_5 structure. Same notations as in Fig. 2.

For $d_h = 400$ nm, the hole only sustains $\ell = \pm 1$, while, with the given $m_{\text{in}} = -1$, the SP topological index $\ell_{\text{SP}} = m_{\text{in}} \pm 1$ will be equal to 0 or -2. In this case, the OAM transmission is a $[\mathsf{C}(m_{\text{out}}) + \mathsf{I}_{\text{out}}]^{\dagger} \cdot \mathsf{H}_{\ell n} \cdot \mathsf{I}_{\text{in}}$ process which corresponds to a summation rule in Table I with $m_{\text{in}} = 0$ and with $m_{\text{out}} = 0$ (the latter being consistent with the BE on the back side). This analysis solves the early paradoxical observations when flipping the BE-R_1 structure.

When d_h reaches 600 nm, the TM_{01} mode is allowed, in addition with the TE_{11} mode. This TM mode can only be excited by the SP field and this time, the selection rule can be fulfilled when $\ell = m_{\text{in}} + 1 = 0$, i.e., when the incident light is $\hat{\boldsymbol{\sigma}}_+$ polarized. In this case, we expect transmitted ± 1 OAM indices in the $(\pm, +)$ subspace. When the incident light is $\hat{\boldsymbol{\sigma}}_-$ polarized, $\ell = m_{\text{in}} - 1 = -2$ is not yet supported by the hole. This makes the interferograms $(\pm, -)$ exhibit indices of -2 and 0 which is, again, expected from $m_{\text{in}} = m_{\text{out}} = 0$ situation.

However an $\ell = -2$ value is allowed once $d_h \geq 740$ nm. The last two columns of Fig. 3 for $d_h = 800$ nm and 1 μm correspond to holes where TE_{21} can be excited. The OAM measurements are fully compatible with Table I with $m_{\text{in}} = -1$ and $m_{\text{out}} = 0$. In short, the OAM cutoff conditions imposed by the central hole take an active part in the far field OAM process we have been describing. In this sense, the relation between the hole and the singularity of the coupled near field evidences the importance of spin-orbit interaction at the level of single apertures [38]. These conditions can be exploited to get a further control over OAM generation as they imply specific designs for the front-side structures. To illustrate this most dramatically, we have prepared an ($L_1 - R_5$, $d_h = 800$ nm) structure. As shown in Fig. 4(b), the L_5 chiral structure consists of five intertwined Archimedean spirals. This suspended structure allows generating, through a TE_{21} waveguide mode, OAM in the far field up to $|\ell| = 8$, again in perfect agreement with the expected OAM summation rules. This value is in strict relation with the chosen structures and is not a limit to our device.

These experiments have revealed important properties of singular plasmonic interactions in the near field. The OAM cutoff conditions related to the aperture are essential in understanding the relation between OAM evolutions and reciprocity, our devices working like plasmon-based OAM optical diodes [41]. Also their versatility makes them easily integrable in 2D plasmonic systems as optical vortex generators useful for optical communication [42]. We thus believe that the concepts discussed here bear a fundamental importance in plasmonics and nanophotonics as well as provide a basis for novel applications in nanotechnology.

The authors acknowledge support from the ERC (Grant No. 227557) and the program Investissement d'Avenir (Equipex Union).

*Corresponding author.
genet@unistra.fr

[1] S. W. Hell, Nat. Methods **6**, 24 (2009).
[2] J. Demas, M. D. W. Grogan, T. Alkeskjold, and S. Ramachandran, Opt. Lett. **37**, 3768 (2012).
[3] M. E. J. Friese, T. A. Nieminen, N. R. Heckenberg, and H. Rubinsztein-Dunlop, Nature (London) **394**, 348 (1998).
[4] G. Molina-Terriza, J. P. Torres, and L. Torner, Nat. Phys. **3**, 305 (2007).
[5] J. B. Pendry, Science **306**, 1353 (2004).
[6] A. R. Parker and H. E. Townely, Nat. Nanotechnol. **2**, 347 (2007).
[7] M. D. Turner, G. E. Schröder-Turk, and M. Gu, Opt. Express **19**, 10001 (2011).
[8] V. A. Fedotov, P. L. Mladyonov, S. L. Prosvirnin, A. V. Rogacheva, Y. Chen, and N. I. Zheludev, Phys. Rev. Lett. **97**, 167401 (2006).
[9] B. Bai, Y. Svirko, J. Turunen, and T. Vallius, Phys. Rev. A **76**, 023811 (2007).
[10] A. Drezet, C. Genet, J.-Y. Laluet, and T. W. Ebbesen, Opt. Express **16**, 12559 (2008).
[11] Y. Tang and A. E. Cohen, Phys. Rev. Lett. **104**, 163901 (2010).

[12] E. Hendry, T. Carpy, J. Johnston, M. Popland, R. V. Mikhaylovskiy, A. J. Lapthorn, S. M. Kelly, L. D. Barron, N. Gadegaard, and M. Kadodwala, Nat. Nanotechnol. **5**, 783 (2010).
[13] M. Hentschel, M. Schäferling, T. Weiss, N. Liu, and H. Giessen, Nano Lett. **12**, 2542 (2012).
[14] V. E. Lembessis, M. Babiker, and D. L. Andrews, Phys. Rev. A **79**, 011806 (2009).
[15] S. Yang, W. Chen, R. L. Nelson, and Q. Zhan, Opt. Lett. **34**, 3047 (2009).
[16] S. Zhang, H. Wei, K. Bao, U. Håkanson, N. J. Halas, P. Nordlander, and H. Xu, Phys. Rev. Lett. **107**, 096801 (2011).
[17] F. Rüting, A. I. Fernández-Domínguez, L. Martín-Moreno, and F. J. García-Vidal, Phys. Rev. B **86**, 075437 (2012).
[18] S.-W. Cho, J. Park, S.-Y. Lee, H. Kim, and B. Lee, Opt. Express **20**, 10083 (2012).
[19] T. Ohno and S. Miyanishi, Opt. Express **14**, 6285 (2006).
[20] Y. Gorodetski, A. Niv, V. Kleiner, and E. Hasman, Phys. Rev. Lett. **101**, 043903 (2008).
[21] Y. Gorodetski, N. Shitrit, I. Bretner, V. Kleiner, and E. Hasman, Nano Lett. **9**, 3016 (2009).
[22] G. Rui, R. L. Nelson, and Q. Zhan, Opt. Lett. **36**, 4533 (2011).
[23] P. Zilio, E. Mari, G. Parisi, F. Tamburini, and F. Romanato, Opt. Lett. **37**, 3234 (2012).
[24] H. J. Lezec, A. Degiron, E. Devaux, R. A. Linke, L. Martín-Moreno, F. J. García-Vidal, and T. W. Ebbesen, Science **297**, 820 (2002).
[25] A. Degiron and T. W. Ebbesen, Opt. Express **12**, 3694 (2004).
[26] M. Sarrazin, J.-P. Vigneron, and J.-M. Vigoureux, Phys. Rev. B **67**, 085415 (2003).
[27] C. Genet, M. P. van Exter, and J. P. Woerdman, Opt. Commun. **225**, 331 (2003).
[28] In order to record the best interferograms, we need to image the transmitted beam slightly behind the membrane where the direct, but diffractive hole transmission is no longer dominant. For all images, this distance is fixed at $\delta z = 20$ μm as shown in Fig. 1(a). Direct transmission can be cancelled by cross-polarizing the transmitted beam with respect to the incident polarization. The interferogram is then replaced by a mere doughnut-shaped beam, as shown in Fig. 1(c). The determination of ℓ from such an image, while still possible, is not as straightforward as from an interferogram. Therefore, we will always project the transmitted beam on a cross-polarized state made slightly elliptical in order to revive the contribution of the direct transmission channel and thus image again the associated interference.
[29] M. Harris, C. A. Hill, and J. M. Vaughan, Opt. Commun. **106**, 161 (1994).
[30] L. Allen, S. M. Barnett, and M. J. Padgett, *Optical Angular Momentum* (Institute of Physics, Bristol, England, 2003).
[31] J.-Y. Laluet, E. Devaux, C. Genet, T. W. Ebbesen, J.-C. Weeber, and A. Dereux, Opt. Express **15**, 3488 (2007).
[32] T. V. Teperik, A. Archambault, F. Marquier, and J. J. Greffet, Opt. Express **17**, 17483 (2009).
[33] See Supplemental Material at http://link.aps.org/supplemental/10.1103/PhysRevLett.110.203906 for mathematical details.
[34] E. Lombard, A. Drezet, C. Genet, and T. W. Ebbesen, New J. Phys. **12**, 023027 (2010).
[35] E. Brasselet, N. Murazawa, H. Misawa, and S. Juodkazis, Phys. Rev. Lett. **103**, 103903 (2009).
[36] L. Marrucci, C. Manzo, and D. Paparo, Phys. Rev. Lett. **96**, 163905 (2006).
[37] A. Yu. Nikitin, D. Zueco, F. J. García-Vidal, and L. Martín-Moreno, Phys. Rev. B **78**, 165429 (2008).
[38] L. T. Vuong, A. J. L. Adam, J. M. Brok, P. C. M. Planken, and H. P. Urbach, Phys. Rev. Lett. **104**, 083903 (2010).
[39] J.-M. Yi, A. Cuche, F. de León-Pérez, A. Degiron, E. Laux, E. Devaux, C. Genet, J. Alegret, L. Martín-Moreno, and T. W. Ebbesen, Phys. Rev. Lett. **109**, 023901 (2012).
[40] J. Kindler, P. Banzer, S. Quabis, U. Peschel, and G. Leuchs, Appl. Phys. B **89**, 517 (2007).
[41] J. Hwang, M. H. Song, B. Park, S. Nishimura, T. Toyooka, J. W. Wu, Y. Takanishi, K. Ishikawa, and H. Takezoe, Nat. Mater. **4**, 383 (2005).
[42] X. Cai, J. Wang, M. J. Strain, B. Johnson-Morris, J. Zhu, M. Sorel, J. L. O'Brien, M. G. Thompson, and S. Yu, Science **338**, 363 (2012).